# *PIK3CA* mutant tumors depend on oxoglutarate dehydrogenase

Nina Ilic[a,b], Kıvanç Birsoy[c], Andrew J. Aguirre[a,b], Nora Kory[b,d,e,f,g], Michael E. Pacold[b,d,e,f,g,1], Shambhavi Singh[a,b], Susan E. Moody[a,b], Joseph D. DeAngelo[a,b], Nicole A. Spardy[a,b], Elizaveta Freinkman[d,2], Barbara A. Weir[a,b], Aviad Tsherniak[b], Glenn S. Cowley[b,3], David E. Root[b], John M. Asara[h], Francisca Vazquez[a,b], Hans R. Widlund[i], David M. Sabatini[b,d,e,f,g], and William C. Hahn[a,b,4]

[a]Department of Medical Oncology, Dana-Farber Cancer Institute, Harvard Medical School, Boston, MA 02215; [b]Broad Institute of MIT and Harvard University, Cambridge, MA 02142; [c]Laboratory of Metabolic Regulation and Genetics, The Rockefeller University, New York, NY 10065; [d]Whitehead Institute for Biomedical Research, Cambridge, MA 02142; [e]David H. Koch Institute for Integrative Cancer Research at MIT, Cambridge, MA 02139; [f]Howard Hughes Medical Institute, Massachusetts Institute of Technology, Cambridge, MA 02139; [g]Department of Biology, Massachusetts Institute of Technology, Cambridge, MA 02139; [h]Department of Medicine, Division of Signal Transduction, Beth Israel Deaconess Medical Center, Harvard Medical School, Boston, MA 02115; and [i]Department of Dermatology, Brigham and Women's Hospital, Harvard Medical School, Boston, MA 02115

Edited by Owen N. Witte, Howard Hughes Medical Institute UCLA, Los Angeles, CA, and approved March 22, 2017 (received for review October 28, 2016)

**Oncogenic *PIK3CA* mutations are found in a significant fraction of human cancers, but therapeutic inhibition of PI3K has only shown limited success in clinical trials. To understand how mutant PIK3CA contributes to cancer cell proliferation, we used genome scale loss-of-function screening in a large number of genomically annotated cancer cell lines. As expected, we found that *PIK3CA* mutant cancer cells require *PIK3CA* but also require the expression of the TCA cycle enzyme 2-oxoglutarate dehydrogenase (OGDH). To understand the relationship between oncogenic PIK3CA and OGDH function, we interrogated metabolic requirements and found an increased reliance on glucose metabolism to sustain *PIK3CA* mutant cell proliferation. Functional metabolic studies revealed that OGDH suppression increased levels of the metabolite 2-oxoglutarate (2OG). We found that this increase in 2OG levels, either by OGDH suppression or exogenous 2OG treatment, resulted in aspartate depletion that was specifically manifested as auxotrophy within *PIK3CA* mutant cells. Reduced levels of aspartate deregulated the malate–aspartate shuttle, which is important for cytoplasmic $NAD^+$ regeneration that sustains rapid glucose breakdown through glycolysis. Consequently, because *PIK3CA* mutant cells exhibit a profound reliance on glucose metabolism, malate–aspartate shuttle deregulation leads to a specific proliferative block due to the inability to maintain $NAD^+$/NADH homeostasis. Together these observations define a precise metabolic vulnerability imposed by a recurrently mutated oncogene.**

PIK3CA | 2OG | OGDH | TCA cycle | glycolysis

Mutations in PI3K, particularly those involving the catalytic subunit PI3Kα, encoded by *PIK3CA*, are found in a number of cancer cell lineages, including breast, colorectal, endometrial, and lung (1). PI3K signaling is normally activated in response to membrane-bound receptor stimulation, which in turn activates several effector molecules that ultimately promote cell proliferation, survival, and motility (2). Mutations in PI3Kα are clustered within the helical (E542K or E545K) or catalytic (H1047R) domain, each of which leads to constitutive kinase activation, hyperactive downstream signaling, and proproliferative cues. Expression of mutant *PIK3CA* in cell or animal models induces tumorigenicity, confirming that these mutations are oncogenic (3).

Multiple PI3K inhibitors have been developed, and both pan-PI3K and PI3Kα-specific inhibitors are the subject of ongoing clinical trials (4). To date, these inhibitors have only shown limited clinical activity (5, 6). Because the mutant PI3Kα isoform appears to be the key driver of tumorigenic phenotypes in genetically engineered mouse models (2), development of mutation-specific PI3Kα inhibitors may lead to improved outcomes.

Although it is clear that oncogenic PI3Kα drives hyperactivity of normal downstream signaling cascades, accumulating evidence indicates that these mutant alleles also exhibit additional activities. Specifically, oncogenic PI3Kα is thought to promote glycolysis by enabling heightened glucose uptake through regulation of GLUT1/4 protein translation (7) and subsequent plasma membrane translocation (8), as well as regulating metabolite pathways (9, 10). However, enhanced glycolysis is also observed in rapidly proliferating cells, which requires increased glucose uptake (11). Consequently, it has been difficult to discern how individual oncogenes affect metabolism, because proliferation alone has broad impact on nutrient demand and utilization.

As an alternative to studies of candidate genes, genome-scale loss-of-function screens offer an unbiased means to discover novel and previously uncharted dependencies and functional relationships in cells. Project Achilles is an effort to identify and characterize cancer cell vulnerabilities by identifying gene dependencies at genome-scale in a large number of human cancer cell lines (12, 13). Using this dataset, we have focused on genes

## Significance

**Oncogenic lesions give rise to genotype-specific dependencies in tumors by altering cell physiology. Understanding how oncogenes drive cell transformation will therefore help identify strategies to target tumors harboring these mutations. Although targeting certain oncogenes has led to clinical responses in some cases, PIK3CA inhibition has been disappointing to date. Here, we show that cell proliferation and tumor growth of *PIK3CA* mutant cancers is inhibited by suppression 2-oxoglutarate dehydrogenase, which leads to increased metabolite 2-oxoglutarate (2OG) levels. Elevated 2OG affects the function of the malate–aspartate shuttle, which is important because of the glycolytic nature of these cancers. This work provides novel insights into how mutant PIK3CA drives tumor proliferation and identifies a metabolic dependency that can be exploited in these cancers.**

Author contributions: N.I., H.R.W., and W.C.H. designed research; N.I., K.B., A.J.A., N.K., S.S., S.E.M., J.D.D., N.A.S., and H.R.W. performed research; E.F., J.M.A., and F.V. contributed new reagents/analytic tools; N.I., A.J.A., M.E.P., E.F., B.A.W., A.T., G.S.C., D.E.R., J.M.A., F.V., H.R.W., D.M.S., and W.C.H. analyzed data; and N.I. and W.C.H. wrote the paper.

Conflict of interest statement: W.C.H. is a consultant for Novartis.

This article is a PNAS Direct Submission.

[1]Present address: Department of Radiation Oncology, New York University Langone Medical Center, New York, NY 10016.

[2]Present address: Metabolon, Inc., Research Triangle Park, NC 27709.

[3]Present address: Discovery Science, Janssen Research and Development (Johnson & Johnson), Spring House, PA 19477.

[4]To whom correspondence should be addressed. Email: william_hahn@dfci.harvard.edu.

This article contains supporting information online at www.pnas.org/lookup/suppl/doi:10.1073/pnas.1617922114/-/DCSupplemental.

that are specifically required for proliferation or survival of cancer cells that bear oncogenic *PIK3CA* mutations. This approach identified the tricarboxylic acid cycle (TCA) cycle enzyme 2-oxoglutarate dehydrogenase (OGDH) as an essential requirement to maintain *PIK3CA* mutant tumor cell proliferation or survival.

## Results

**Identification of OGDH as a Dependency Associated with *PIK3CA* Mutation.** To identify genes and pathways that are required in cancer cells that harbor *PIK3CA* mutations, we used genome-scale shRNA data from Project Achilles (12, 13). Specifically, we used data derived from screening 17 *PIK3CA* mutant (MUT class) and 68 *PIK3CA* wild-type (WT class) cell lines, where individual covariant shRNA values (from a pool of ≥5 shRNAs per gene) were condensed to gene level dependencies using ATARiS (14). We then performed a two-class (MUT vs. WT) comparison among the two cell line classes by computing rescaled and normalized mutual information (RNMI) scores using the PARIS module in GenePattern (13) (Fig. 1*A*). To identify pathways or cell processes that represent specific vulnerabilities in *PIK3CA* MUT cells, we then performed Gene Set Enrichment Analysis (GSEA) (15) using the highest probability ranked genes, which revealed an enrichment for gene sets associated with the spliceosome, the TCA cycle, and lysine degradation (Fig. 1*B*). As expected, the gene with the highest association to the *PIK3CA* MUT class was *PIK3CA* (12) (Fig. 1*C* and Dataset S1). Among the 25 highest-ranked dependencies, we found all three components of the OGDH complex, including OGDH, dihydrolipoamide S-succinyltransferase (DLST), and dihydrolipoamide dehydrogenase (DLD) (Fig. 1 *C* and *D*) (16). OGDH is a highly conserved TCA mitochondrial enzyme complex that catalyzes the irreversible conversion of 2-oxoglutarate (2OG) and CoA-SH to succinyl–CoA and $CO_2$, while reducing $NAD^+$ to yield NADH (16).

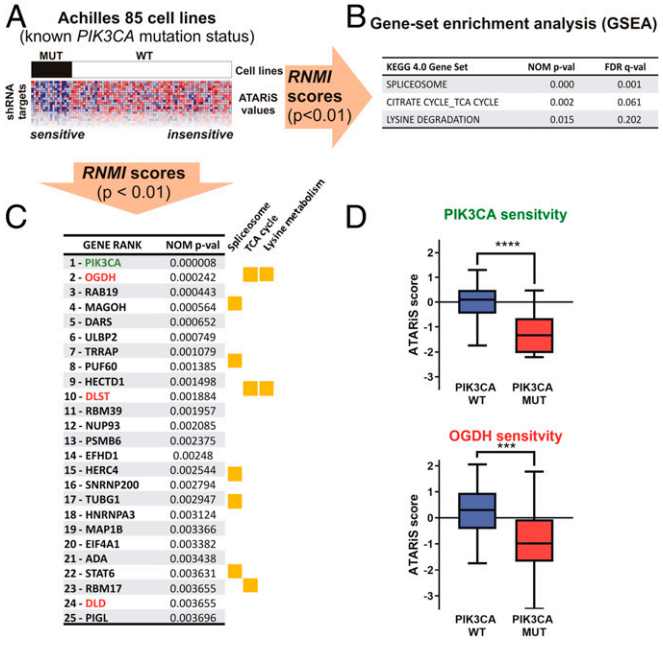


**Fig. 1.** Genome-scale loss-of-function analyses identify the OGDH complex as a dependency in *PIK3CA* MUT cell lines. (*A*) Two-class comparative analysis of combined gene-level shRNA scores (ATARiS values) between *PIK3CA* MUT and WT cancer cell lines using PARIS module RNMI statistics for genes required for *PIK3CA* MUT cells ($P < 0.01$) used for (*B*) pathway identification by GSEA (FDR < 0.25, $P < 0.01$) and (*C*) gene rank list of top 25 *PIK3CA* mutation-associated dependencies. (*D*) Average ATARiS score sensitivity among *PIK3CA* WT ($n = 68$) and MUT ($n = 17$) cell lines for PIK3CA and OGDH (***$P < 0.001$; ****$P < 0.0001$ calculated using an unpaired two-sided *t* test).

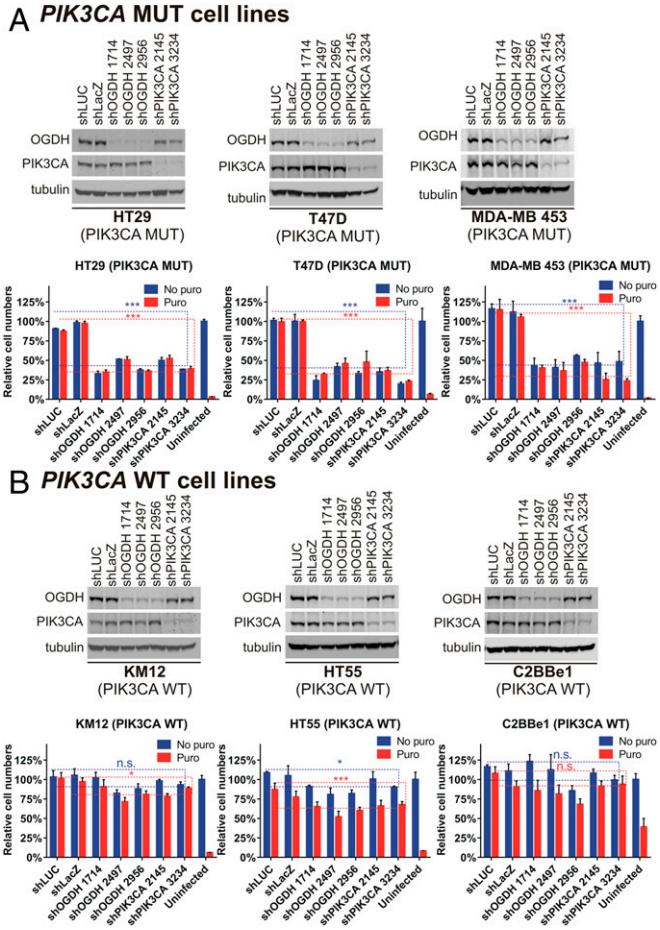


**Fig. 2.** Differential effects of *OGDH* and *PIK3CA* suppression on *PIK3CA* MUT and WT cell lines. (*A* and *B*) Matched immunoblot and proliferation assays for *PIK3CA* MUT (*A*) and WT (*B*) cell lines following shRNA suppression of *OGDH* and *PIK3CA*. Proliferation assays in the absence (blue bars) or presence (red bars) of shRNA-selectable marker puromycin (puro). Proliferation data presented as the mean of four replicates + SD; *P* values calculated using an unpaired two-sided *t* test (all shCONTROL vs. all shOGDH and shPIK3CA; *$P < 0.05$, **$P < 0.01$, ***$P < 0.001$).

To validate these observations, we individually assessed *OGDH* (Fig. 2 and Fig. S1*A*), *DLST* (Fig. S2*A*), *DLD* (Fig. S2*B*), and *PIK3CA* (Fig. 2 and Fig. S1*A*) as dependencies in multiple *PIK3CA* MUT and WT cell lines. Using at least two individual shRNAs per gene, we confirmed that these shRNAs suppressed the expression of each of these genes independent of mutation status (Fig. 2 and Figs. S1*B* and S2) and found that cell lines harboring *PIK3CA* MUT uniquely depended on each of the OGDH complex components for proliferation/survival.

**OGDH Is Necessary to Maintain Mutant *PIK3CA* Tumor Growth in Vivo.** Because the genes and pathways used by cells grown in culture may differ from genes required to sustain tumor growth in vivo, we investigated whether OGDH suppression affects tumor xenograft growth. We engineered *PIK3CA* MUT (RKO and HCT116) and WT (LS411N and HT55) cancer cell lines to express doxycycline (dox)-inducible shRNAs targeting OGDH and controls targeting GFP/RFP. Dox treatment induced shRNA suppression of OGDH (Fig. S3 *A* and *B*) and inhibited the proliferation of *PIKC3A* MUT cells in vitro (Fig. S3 *C* and *D*). To validate that these observations were due to on-target effects

of these shRNAs, we generated and introduced a variant OGDH cDNA allele (OGDH wobble) carrying silent mutations within the targeting motifs for each of the three shRNAs (Fig. S3*E*). Compared with controls, expression of this OGDH wobble allele rescued the effects of the OGDH-specific shRNAs (Fig. S3*F*).

To investigate whether OGDH suppression induced a proliferative arrest or cell death in *PIK3CA* MUT cells, we used the fluorescent nucleic acid stain, SYTOX, which does not permeate live cells, thus staining only dead cells. By quantifying SYTOX-positive cells, we failed to detect cell death following OGDH suppression (Fig. S3*G*). We confirmed these observations using trypan blue staining of cells and quantifying cell numbers following shRNA induction (Fig. S3*H*). To assess whether *OGDH* suppression affects the cell cycle, we performed BrdU labeling experiments and found that *PIK3CA* MUT, but not WT, lines exhibit a decrease in BrdU incorporation following OGDH suppression (Fig. S3*I*), suggesting a block in the cell cycle, similar to the effects of pharmacological PI3K inhibition (17).

To examine the requirement for OGDH for *PIK3CA* mutant tumor growth, we implanted the dox-inducible cell lines into immunocompromised mice and induced the expression of the shRNAs either at time of implantation (Fig. 3 *A*–*C*) or subsequent to tumor formation (Fig. 3 *D*–*F*). Confirming our in vitro observations, *PIK3CA* MUT xenografts displayed a significant suppression of tumor growth upon OGDH shRNA induction ($P < 0.01$; Fig. 3 *B* and *E*), whereas suppression of OGDH had no effect on *PIK3CA* WT xenograft tumors (Fig. 3 *C* and *F*). Taken together, these data indicate that OGDH is a genuine dependence in *PIK3CA* mutant cancer cells supporting proliferation.

***PIK3CA* Mutant Cell Lines Display an Enhanced Requirement for Glucose Metabolism.** We next examined how OGDH function affects *PIK3CA* mutant cancer cell proliferation. OGDH is an integral component of the TCA cycle, and the PI3K/mTOR pathway has been suggested to regulate both glucose (7, 8) and glutamine metabolism (18, 19). Hence, we examined the dependence of the *PIK3CA* MUT and WT lines on limiting availability of these two nutrients. Although we found that glutamine deprivation similarly affected proliferation of both *PIK3CA* MUT and WT cells (Fig. 4*A*), reducing glucose availability preferentially affected *PIK3CA* MUT cell line proliferation (Fig. 4*B*). These observations clearly suggested that *PIK3CA* MUT cell lines exhibit a higher

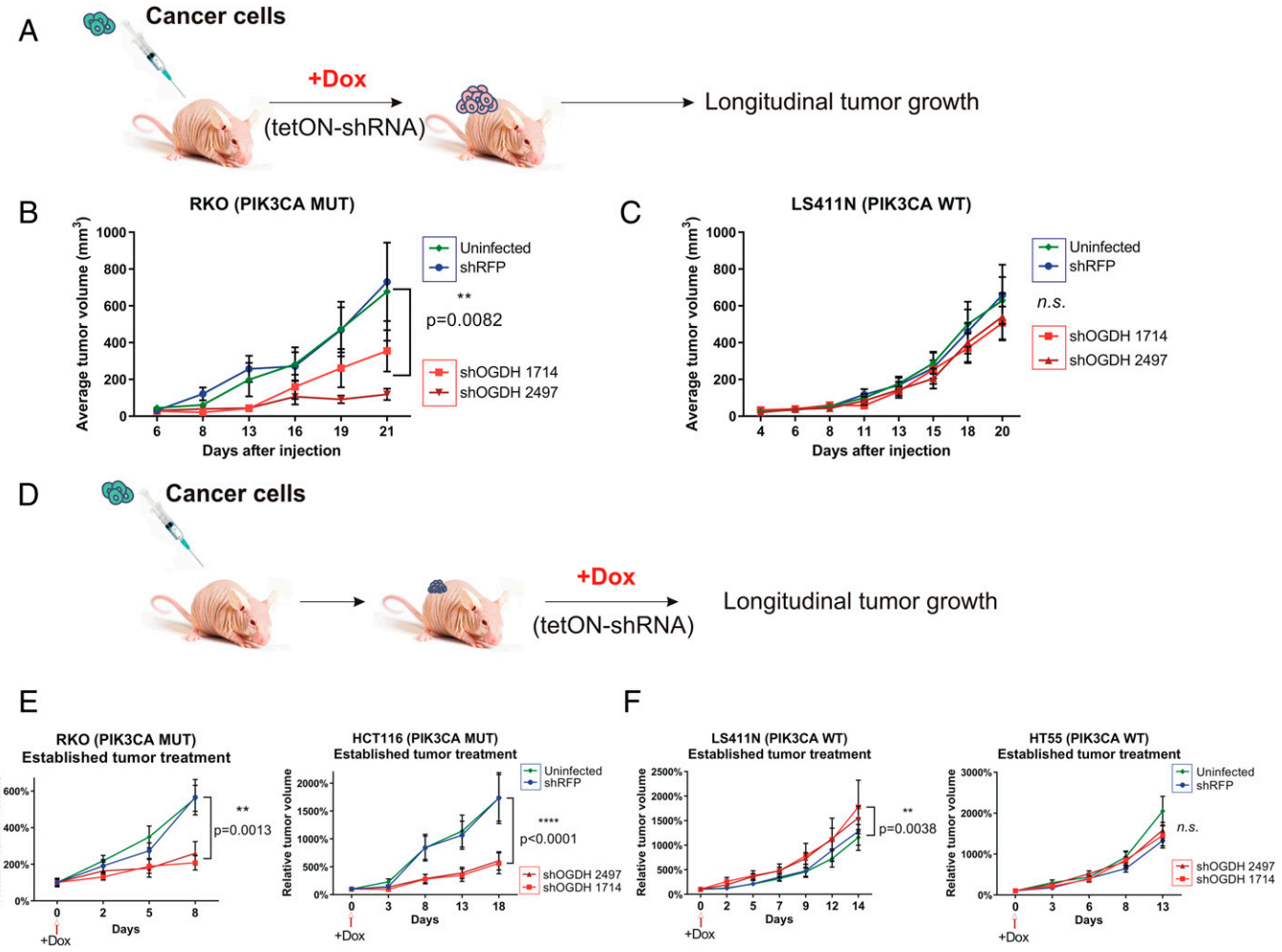


**Fig. 3.** OGDH is an in vivo dependency in *PIK3CA* MUT cell lines. (*A*) Experimental strategy for *B* and *C*. Cancer lines expressing dox-inducible shRNAs were s.c. injected into nude mice and dox was administered on the day of injection; longitudinal tumor growth was monitored over time. (*B* and *C*) *PIK3CA* MUT (*B*) and WT (*C*) xenograft tumor growth following OGDH suppression. Error bars represent SEM for each point; $n = 22$–29 tumors per experimental cohort (all control tumors vs. all shOGDH tumors). (*D*) Experimental strategy for *E* and *F*. Cancer cell lines expressing dox-inducible shRNAs were s.c. injected into nude mice and upon palpable tumor formation dox was administered; longitudinal tumor growth was monitored over time. (*E* and *F*) Xenograft tumor growth of *PIK3CA* MUT (*E*) or WT (*F*) cancer cell lines following induction of shRNAs after palpable tumor formation. Error bars represent SEM for each point; $n = 19$–26 tumors per experimental cohort (all control tumors vs. all shOGDH tumors). *P* values calculated using an unpaired two-sided *t* test (*$P < 0.05$, **$P < 0.01$, ***$P < 0.001$, ****$P < 0.0001$).

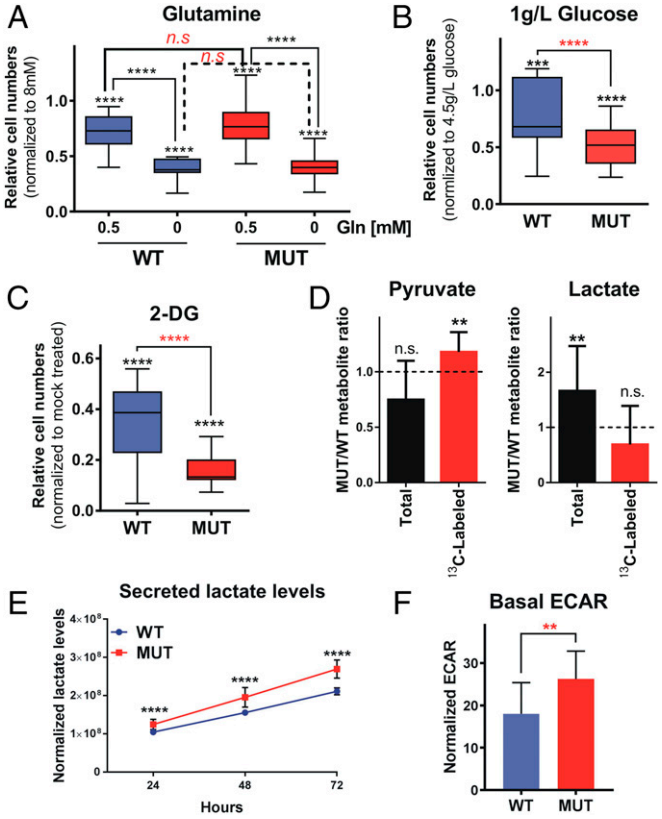


**Fig. 4.** *PIK3CA* MUT cells exhibit higher reliance on glucose. (*A*–*C*) Comparative proliferation effects among *PIK3CA* MUT (AGS, TOV21G, GP2D, RKO, DLD1, HCT116, HT29) and WT (HT55, COV362, KM12, C2BBe1, LS411N) lines propagated for 96 h in (*A*) reduced glutamine media (proliferation in 0.5 mM or no glutamine normalized to 8 mM glutamine); (*B*) reduced glucose media (proliferation in 1 g/L normalized to 4.5 g/L); (*C*) 5 mM 2DG (proliferation with 5 mM 2DG normalized to mock treated). (*D*) Ratio of total and $^{13}$C-labeled pyruvate or lactate in MUT (HCT116, RKO, HT29) vs. WT (HT55, C2BBe1, LS411N) cell lines. (*E* and *F*) Extracellular lactate levels (*E*) and basal ECAR measurements (*F*) in *PIK3CA* MUT (HCT116, RKO, HT29) and WT (HT55, C2BBe1, LS411N) cell lines. $*P < 0.05$, $**P < 0.01$, $***P < 0.001$, $****P < 0.0001$; *P* values were determined by a one-way ANOVA (*A*–*C*) or an unpaired two-sided *t* test (*D*–*F*). Error bars represent SD of the mean of four replicates (*A*–*C*, *E*, and *F*) or three replicates (*D*).

glucose requirement to sustain proliferation, which is in agreement with previous studies (8, 20). To confirm these findings, we measured sensitivity to 2-deoxyglucose (2DG), a competitive inhibitor of the first step of glycolysis [conversion of glucose to glucose-6-phosphate (G6P)] (Fig. 4*C*). We found that that the *PIK3CA* MUT cell lines exhibited higher sensitivity to 2DG compared with the WT cells, paralleling their requirement for higher glucose concentration (Fig. 4*B*). Elevated glycolytic demand could point toward reduced reliance on oxidative phosphorylation; therefore, we examined whether complex I inhibitors rotenone and phenformin (Fig. S4 *A* and *B*), complex V/ATP synthase inhibitor oligomycin A (Fig. S4*A*), and a mitochondrial proton gradient uncoupler 2,4-dinitrophenol (2,4-DNP; Fig. S4*C*) also affected proliferation. These inhibitors affected proliferation nearly uniformly across the cell lines, but independent of *PIK3CA* mutation status. In addition, we measured oxygen consumption rates among *PIK3CA* MUT and WT cell lines (Fig. S4 *D* and *E*) but failed to observe significant differences between the two groups. Hence, it is unlikely that the sensitivity to OGDH suppression in *PIK3CA* mutant cells is due to differences in mitochondrial bioenergetics but rather a consequence of their increased reliance on glucose metabolism.

To investigate the source of differential nutrient use between *PIK3CA* MUT and WT cell lines, we used [U-$^{13}C_6$]–glucose or [U-$^{13}C_5$]–glutamine in media lacking the labeled nutrient. After allowing cells to proliferate for 6 or 7 h, respectively, we performed LC-MS to assess fractional labeling of metabolites. In glutamine-labeled cells, we failed to find consistent differences in steady-state glutamine-to-TCA flux between *PIK3CA* MUT and WT cell lines (shOGDH-sensitive vs. resistant; Fig. S4 *F* and *G*). This finding suggested that utilization or activity of OGDH reaction did not explain the observed differential sensitivity to OGDH suppression. In glucose-labeled cells, however, we observed consistent increases in labeling along the three branches downstream of G6P—glycolysis (pyruvate), pentose phosphate pathway (adenosine and uridine), and nucleotide sugar metabolism (UDP-D-glucuronate; Fig. 4*D* and Fig. S5 *A* and *B*) across the *PIK3CA* mutant cancer cell lines. In addition, total levels of lactate were higher in MUT cells (with no significant difference in fractional labeling; Fig. 4*D*), suggesting altered glucose utilization and flux between pyruvate and lactate. We also found that secreted lactate levels were consistently higher in the MUT cell lines compared with WT measured over 72 h (Fig. 4*E*), as were their basal extracellular acidification rates (ECAR; Fig. 4*F*). When we propagated cells in the presence of the *PIK3CA*-specific catalytic inhibitor, BYL719 (21) at a dose that discriminates between *PIK3CA* MUT and WT cell lines (Fig. S5*C*), we found that total levels of glucose-derived metabolites involved in glycolysis and pentose phosphate pathway were generally reduced in both MUT and WT cells, with overall more potent effects in MUT cells (21) (Fig. S5*D*). Collectively, these data suggest that PIK3CA MUT cancer cells exhibit an enhanced requirement and utilization of glucose.

**Effects of Suppressing OGDH on Metabolic Pathways.** To examine the metabolic consequences of OGDH suppression, we performed LC-MS metabolite profiling following suppression of OGDH in *PIK3CA* MUT and WT cells (Fig. 5 *A* and *B*). In both *PIK3CA* MUT and WT cells, OGDH suppression resulted in a comparable increase in the levels of its substrate, 2OG (Fig. 5*C*), and an expected decrease in the pools of TCA cycle metabolites fumarate, malate, and aspartate (Fig. 5*D*). Furthermore, several metabolites involved in transamination reactions with 2OG (2-oxobutanoate, phenylpyruvate and 2-ketoisovalerate), or products from reactions that use 2OG (acetoacetate), were also affected. Expression of the OGDH wobble allele (Fig. S3 *E* and *F*) reversed these changes (Fig. S6 *A*–*F*).

In addition, we observed that the $NAD^+$/NADH ratio was reduced following OGDH suppression in the sensitive *PIK3CA* MUT cells, indicative of an altered redox state that paralleled sensitivity to OGDH (Fig. 5*E*). NADH produced in the cytosol must be regenerated to $NAD^+$ for glycolysis to proceed, which can be achieved through the activity of lactate dehydrogenase (22–24), glycerol-3-phosphate shuttle (25), or the malate–aspartate shuttle. The malate–aspartate shuttle activity regenerates $NAD^+$ in the cytosol, which brings the reducing equivalents into the mitochondria (26, 27) (Fig. 5*F*). The direct relationship between the malate–aspartate shuttle and OGDH is through the substrate 2OG, which is consumed by transamination reactions on both sides of the mitochondrial membrane (Fig. S7*A*) (27).

To specifically examine the effects of increasing 2OG levels (Fig. 5*C*), we treated *PIK3CA* WT and MUT cells with a membrane-permeable 2OG-ester derivative, dimethyl-(dm)-2OG (28, 29) and assessed effects on cell proliferation. We confirmed an increase in intracellular 2OG levels, and also decreased levels of aspartate (Fig. 5*G*), both of which were comparable to what we observed when we suppressed OGDH (Fig. 5 *C* and *D*). The levels of malate and fumarate remained unaffected (Fig. S6 *G* and *H*), consistent with cytosolic delivery of dm-2OG. In consonance with these observations, we found that dm-2OG treatment potently suppressed the proliferation of *PIK3CA* MUT cells, but had more

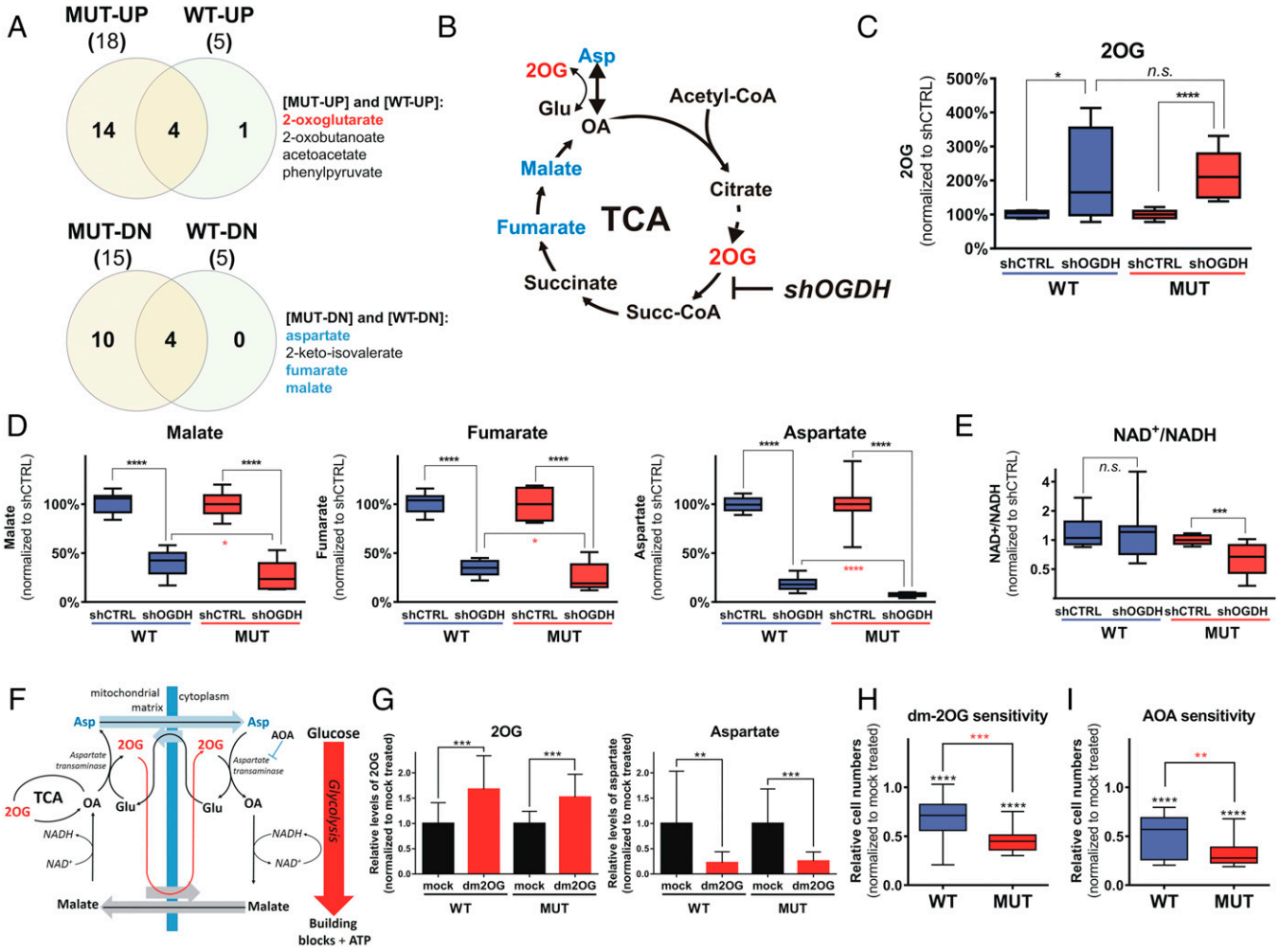


**Fig. 5.** Metabolic effects following OGDH suppression. (*A*) Venn diagrams depicting overlapping metabolite level changes following OGDH suppression in *PIK3CA* WT (HT55, C2BBe1) and MUT (RKO, HT29) cell lines. (*B*) Schematic of the TCA cycle with emphasis on overlapping metabolites whose levels are altered following OGDH suppression (blue, decreased; red, increased). (*C–E*) Relative levels of 2OG (*C*), malate, fumarate, and aspartate (*D*), or $NAD^+$/NADH ratio (*E*) following OGDH suppression. (*F*) Schematic representation of the cytoplasmic–mitochondrial malate–aspartate shuttle that regenerates cytoplasmic $NAD^+$ to enable glycolysis to proceed. (*G*) MS analysis of metabolite changes in *PIK3CA* WT (C2BBe1, COV362, LS411N, HT55) or MUT (TOV21G, DLD1, HCT116, HT29) lines mock treated or propagated in 7 mM dm-2OG for 72 h; relative levels (normalized to mock treated) of 2OG and aspartate are shown; H. Proliferation effects in *PIK3CA* WT (C2BBe1, KM12, HT55, LS411N, COV362) and MUT (HT29, GP2D, TOV21G, RKO, HCT116, DLD1) lines following 96 h treatment with 7 mM dm-2OG. (*I*) Proliferation effects in *PIK3CA* WT (C2BBe1, KM12, HT55, LS411N, COV362) and MUT (AGS, HT29, GP2D, TOV21G, RKO, HCT116, DLD1) lines following 96-h treatment with 1.75 mM AOA. OA, oxaloacetate; Succ-CoA, succinyl-CoA. $*P < 0.05$, $**P < 0.01$, $***P < 0.001$, $****P < 0.0001$. *P* values were determined by an unpaired *t* test with Welch's correction (*C–E* and *G*) or a one-way ANOVA with multiple comparisons (*H* and *I*). Error bars represent SD of the mean of three (*C–E* and *G*) or four replicates (*H* and *I*).

moderate effects on the WT cells (Fig. 5*H*). To confirm the specificity of proliferative effects observed by dm2OG treatment, we treated cells with two additional TCA cycle metabolite esters, dimethyl succinate and diethyl malate, and did not observe differential proliferative suppression among the MUT and WT group (Fig. S6 *I* and *J*).

Because an increase in 2OG levels, either by shOGDH or dm-2OG, preferentially affected *PIK3CA* MUT cell proliferation, we examined whether transamination reactions linked to the malate–aspartate shuttle were affected by these manipulations (Fig. 5*F* and Fig. S7*A*). Specifically, we treated cells with aminooxyacetic acid (AOA), a transaminase inhibitor that exhibits some preferential inhibition of aspartate transaminase (Fig. 5*F*) (27, 30) and subsequently assessed effects on cell proliferation. We found that AOA preferentially suppressed proliferation of the *PIK3CA* MUT cells (Fig. 5*I*). In addition, low-dose AOA sensitized *PIK3CA* WT cell lines to OGDH suppression (Fig. S6 *K* and *L*), indicating that further decrease in aspartate transaminase-mediated oxaloacetate-to-aspartate transamination affects OGDH sensitivity as observed in *PIK3CA* MUT cells. Together, these data show that OGDH suppression causes an expected increase in the levels of 2OG, accompanied by a decrease in the levels of downstream TCA cycle metabolites, as well as a concomitant reduction in $NAD^+$/NADH ratios. These changes are consistent with an altered redox state that can be explained as a consequence of malate–aspartate shuttle transamination reaction inhibition driven by increased 2OG levels (Fig. 5*F*).

**OGDH Suppression Results in Malate and Aspartate Insufficiency.** To gain further insight into acute metabolic changes following OGDH suppression, we performed a 3-h pulse with [U-$^{13}C_6$]–glucose tracer in *PIK3CA* WT and MUT cells to assess effects on glucose-derived metabolites (Fig. S5*A*). We found that labeled glucose-derived lactate and glyceraldehyde-3-phosphate were reduced specifically in *PIK3CA* MUT cells following OGDH

suppression (Fig. S6 *M* and *N*), suggestive of impaired glycolytic flux. As an alternative means to examine the effects on glutamine-derived metabolites, we also used a 7-h pulse with [U-$^{13}C_5$]–glutamine to label cells (Fig. 6*A* and Fig. S4*F*). We found that C5-glutamine incorporation was increased upon OGDH suppression (Fig. S6*O*), suggesting increased reliance on glutamine anaplerosis to sustain the TCA cycle and a shift toward elevated glutaminolysis. As expected, we found a marked increase in total 2OG levels upon OGDH suppression (Fig. 6*B*), accompanied by a 30–50% decrease in one-, two-, and three-carbon labeled (C1, C2, and C3) fractions of 2OG in MUT cells (Fig. 6*C*). Furthermore, we observed a shift toward reductive carboxylation of 2OG toward citrate, reflected in an increase in the C5-labeled fraction, in both of the MUT cell lines, but only one of the WT lines, LS411N (Fig. S6*P*) (31). Despite the threefold increase in C5-labeled citrate observed in MUT cells, this species constituted only ~1–6% of total citrate, suggesting that this alternate path of glutamine-derived carbons likely does not explain sensitivity to OGDH suppression. In agreement with our previous experiments (Fig. 5*D*), we confirmed the reduction in total malate levels in *PIK3CA* MUT cells upon OGDH suppression (Fig. S6*Q*), with more potent reduction in the C1 and C2 fractions in MUT cells (Fig. 6*D*). We also confirmed reduction in total aspartate levels (Fig. 5*D* and Fig. S6*R*), accompanied by more potent decrease in labeled species in MUT cells (Fig. 6*E*).

**OGDH Suppression Induces Aspartate Auxotrophy in *PIK3CA* Mutant Cells.** Given the profound and consistent decrease in aspartate levels caused both by OGDH suppression (Fig. 5*D* and Fig. S6*R*) and exogenous 2OG (Fig. 5*G*), we considered whether depletion of this amino acid following OGDH suppression drives the observed sensitivity in *PIK3CA* MUT cells. Aspartate is a nonessential

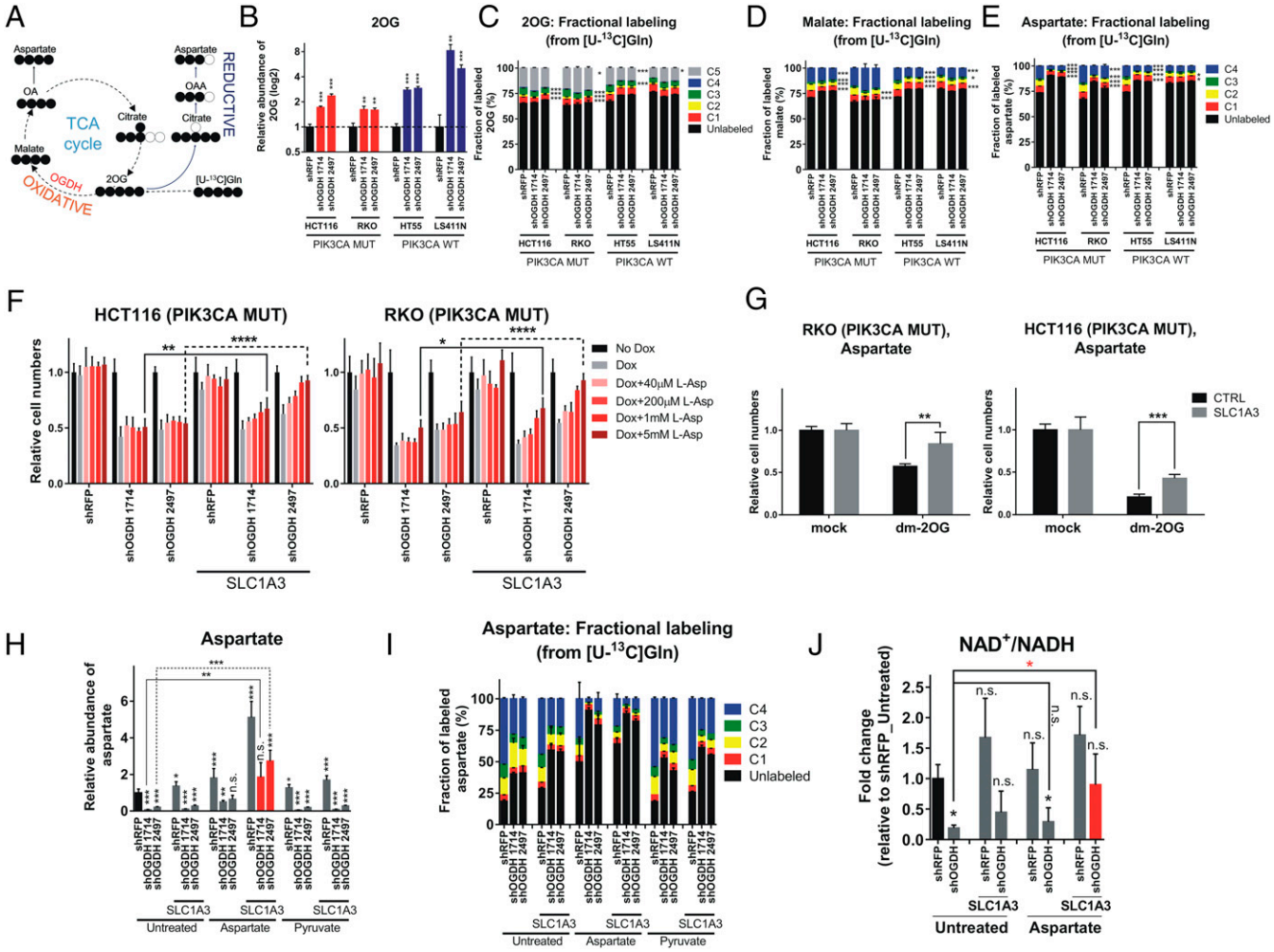


**Fig. 6.** Aspartate supplementation reduces sensitivity to OGDH suppression or 2OG treatment. (*A*) Diagram of anaplerotic glutamine flux into the TCA cycle, depicting both oxidative and reductive pathways of aspartate generation from 2OG. Filled circles depict $^{13}C$ atoms originating from [U-$^{13}C_5$]–L-glutamine. (*B–E*) MS analysis in *PIK3CA* MUT (HCT116 and RKO) and WT (HT55 and LS411N) cell lines cultured in the presence of dox for 72 h and with [U-$^{13}C_5$]–glutamine for 7 h; total pool sizes for 2OG (*B*) are shown separately from fractions of glutamine-derived labeled 2OG (*C*), malate (*D*), and aspartate (*E*). (*F*) Proliferation assay for *PIK3CA* MUT cell lines (HCT116 and RKO) expressing dox-inducible shRNAs, without or with ectopic SLC1A3, 96 h post dox induction of shRNAs and concurrent addition of L-aspartate. (*G*) Proliferation of *PIK3CA* MUT cell lines (RKO and HCT116) overexpressing SLC1A3, in the presence of 10 mM aspartate and mock treated or treated with 5 mM dm-2OG for 96 h. (*H* and *I*) MS analysis of aspartate in *PIK3CA* MUT cell line RKO expressing dox-inducible shRNAs, without or with ectopic SLC1A3. Cells were cultured in the presence of dox with or without 5 mM L-aspartate or 1 mM sodium pyruvate for 72 h and with [U-$^{13}C_5$]–glutamine for 7 h. Total pool sizes for aspartate (*H*) are shown separately from fractions of glutamine-derived labeled aspartate (*I*). (*J*) MS analysis of $NAD^+$/NADH ratios in *PIK3CA* MUT cell line RKO. Cells were cultured in the presence of dox with or without 5 mM L-aspartate for 72 h. Each bar represents the mean + SD of three (*B–E* and *H–J*) or four (*F* and *G*) replicates. $^*P < 0.05$, $^{**}P < 0.01$, $^{***}P < 0.001$, $^{****}P < 0.0001$. *P* values were determined by unpaired two-tailed *t*-test statistics with Welch's correction for unequal variance (*B–E*), unpaired two-tailed *t* test (*G*), or a one-way ANOVA (*F* and *H–J*).

amino acid that is generated in the cell through 2OG-dependent transamination to and from oxaloacetate (Fig. S7*A*). Following OGDH suppression in *PIK3CA* MUT cells, reduced aspartate levels (Fig. 5*D* and Fig. S6*R*) could be caused by mitochondrial 2OG accumulation and matrix-side malate–aspartate shuttle deregulation (Fig. 5*F*) (32), and conversely exogenous 2OG addition would result in the same changes but initiated on the cytoplasmic side. Interestingly, in mitochondrial respiration deficient cells, or in the presence of complex I inhibitor phenformin, aspartate supplementation was recently shown to support cell proliferation and bypass oxidative phosphorylation inhibition as well as genetic defects in mitochondrial DNA (33, 34). To assess whether aspartate supplementation could reduce sensitivity to OGDH suppression, we used high-dose aspartate supplemented media and measured cell proliferation. We found that exogenous addition of aspartate could not restore proliferation (Fig. S7*B*). This result was, however, not surprising, given that most tissues outside the CNS do not normally express aspartate transporters at the plasma membrane (33). However, ectopic expression of the aspartate/glutamate transporter, SLC1A3 (33) (Fig. S7*C*), in combination with aspartate supplementation, caused a robust and dose-dependent sensitivity decrease to OGDH suppression (Fig. 6*F*). Furthermore, overexpression of SLC1A3 in the presence of exogenous aspartate reduced sensitivity to exogenous dm-2OG (Fig. 6*G*), suggesting that intracellular 2OG increases drive differential OGDH sensitivity. Notably, pyruvate supplementation following OGDH suppression did not reduce sensitivity (Fig. S7*D*), likely because aspartate generated from oxaloacetate, which originates from malate or anaplerotically from pyruvate, requires a transamination that is imbalanced due to excess 2OG (Fig. S7*A*).

**Aspartate Supplementation Restores a Truncated TCA Cycle.** To assess which metabolic pathways were restored by aspartate supplementation, we performed [U-$^{13}C_5$]–glutamine tracer experiments (Fig. 6*A* and Fig. S4*F*). As expected, we confirmed that aspartate and malate levels were restored following aspartate, but not pyruvate, addition (Fig. 6 *H* and *I* and S7*G*), whereas 2OG and succinate levels remained elevated and depleted, respectively (Fig. S7 *E* and *F*). In addition, aspartate supplementation restored the $NAD^+$/NADH ratio upon OGDH suppression to that of unperturbed control (Fig. 6*J*). These observations collectively indicate that the shOGDH-induced truncation of the TCA cycle causes 2OG to deplete malate and aspartate, both because of the effects on the TCA cycle but also due to affecting the operation of the malate–aspartate shuttle. Because of its important role in $NAD^+$ regeneration for sustained glycolysis and maintained building-block synthesis, the malate–aspartate shuttle function is more critical for *PIK3CA* mutant cancer cell lines (Figs. 5*F* and 7 and Fig. S7*H*), leading to differential dependency on OGDH function to maintain intracellular 2OG balance.

## Discussion

Mutations in metabolic genes, such in IDH1/2 (35), fumarate hydratase (36), succinate dehydrogenase (37, 38), and mitochondria-encoded genes (39), although relatively rare, are actively pursued for therapy because of their causal involvement in the tumors that carry those lesions. In addition, hallmark oncogenes such as *KRAS* (40, 41) and *MYC* (42), as well as the mTORC1 pathway (18), provoke unique metabolic dependencies when hyperactivated. Because of their frequent involvement in promoting cancer development and growth, these dependencies are therefore being considered for improving cancer treatment.

From genome-scale vulnerability screens, we have identified the mitochondrial TCA cycle enzyme OGDH as a specific vulnerability in *PIK3CA* mutant cancer cells, required both for proliferation in culture, as well as in vivo tumor maintenance (Fig. S3 and Fig. 3). The PI3K pathway has previously been associated with multiple roles in metabolism, involving heightened

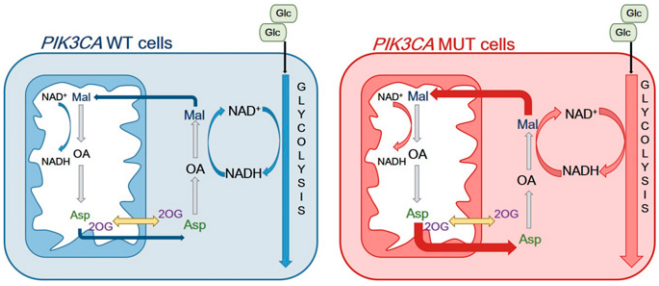


**Fig. 7.** Model depicting increased requirement of *PIK3CA* MUT cell lines for unperturbed operation of the malate–aspartate shuttle to satisfy their heightened glycolytic needs for $NAD^+$ regeneration. OGDH suppression causes 2OG increase, which in turn depletes aspartate availability, causing a disruption in malate–aspartate shuttle operation.

glucose import through regulation of GLUT1 expression; GLUT4 translation and membrane localization (7, 8); stimulation of glutathione synthesis (43); and suppression of β-oxidation (9). In our analyses, and akin to previous reports (44), PIK3CA mutant cells do not exhibit altered reliance on mitochondrial metabolism (Fig. S4), suggesting an alternative requirement for OGDH, other than its role in the TCA cycle.

Using metabolomic and pharmacological approaches, we found that *PIK3CA* mutant cancer cells rely on OGDH through maintaining appropriate levels of the substrate 2OG. Following inhibition of OGDH, 2OG levels are increased (Figs. 5*C* and 6*B*), whereas the levels of malate and aspartate decrease (Fig. 5*D* and Fig. S6 *Q* and *R*), which in *PIK3CA* mutant cells reduces the $NAD^+$/NADH ratio (Fig. 5*E* and Fig. S6*F*). In keeping with these results, it was recently reported that certain cancer cell lines depend on OGDH activity for aspartate and function of the malate–aspartate shuttle (45); however, without any association with tumor cell mutation status. The glycolytic nature of *PIK3CA* mutant cells, reflected in their reliance on glucose (Fig. 4*B*), sensitivity to inhibition of glycolysis (Fig. 4*C*), and elevated secretion of lactate (Fig. 4 *E* and *F*), collectively imparts sensitivity to excess 2OG levels via deregulation of malate–aspartate shuttle activity, an important $NAD^+$ regeneration pathway in the cytoplasm (Fig. 5*F*). Our observations suggest that dependence on OGDH activity is increased in cells with elevated glucose demand. Thus, we provide mechanistic insight into why a defined subset of cancer cell lines are more dependent on OGDH function through their heightened reliance on 2OG maintenance, which closely associates with the highlighted role of PIK3CA in promoting anabolic metabolism (7–10).

Inherent stress from uncontrolled cancer cell growth provokes metabolic insufficiencies that must be satisfied by alternative nutrient uptake for TCA cycle catabolism, which involves β-oxidation of lipids, increased glutaminolysis, and breakdown of extracellular proteins. To this end, *PIK3CA* mutant colorectal cancer cell lines were recently shown to up-regulate the glutamate pyruvate transaminase 2 (*GPT2*) to fuel the TCA cycle with 2OG generated from pyruvate and glutamate (46). Notably, this role for GPT2 within *PIK3CA* mutant colon cancer cells was determined under glutamine depletion; this represents an alternative pathway for pyruvate and glutamate to sustain the TCA cycle that would parallel the widely appreciated anaplerotic roles of pyruvate to generate oxaloacetate through pyruvate carboxylase and glutamate dehydrogenase to generate 2OG. In our experiments, conducted in complete media, OGDH suppression or exogenous 2OG addition, we failed to find deregulation of the TCA cycle attributable to PIK3CA mutation (Fig. 5*G* and Fig. S6 *G* and *H*). Importantly, we found that the effects of OGDH suppression or 2OG treatment were alleviated by increasing intracellular levels of aspartate using aspartate/glutamate transporter overexpression and exogenous aspartate supplementation

(Fig. 6 *F* and *G*). Aspartate supplementation following OGDH suppression, however, did not restore the levels of the TCA cycle metabolites 2OG and succinate (Fig. S7 *E* and *F*), but restored the $NAD^+$/NADH ratios (Fig. 6*J*) and cell proliferation (Fig. 6 *F–I* and Fig. S7 *G* and *H*). These observations suggest that it is the effects of elevated 2OG on depleting aspartate, rather than general suppression of the TCA cycle, that represents a unique vulnerability in *PIK3CA* mutant cells.

We speculate that pyruvate anaplerosis via oxaloacetate does not occur because aspartate is made from oxaloacetate, and this reaction is opposed by elevated 2OG (Fig. S7*A*). Because PIK3CA mutant cell lines require $NAD^+$ regeneration due to their inability to regulate glycolytic flux, our findings point toward 2OG imbalance as a critical metabolic sensitivity in this class of cancers. Although aspartate is integral to the operation of the malate–aspartate shuttle, we note that it is also a required metabolite for additional metabolic pathways, including the urea cycle (47); nucleotide synthesis (48–50); arginine (51) and asparagine synthesis (52); glutamate metabolism (53); and protein synthesis (54). Hence, it is possible that additional pathways in the *PIK3CA* MUT cancers also require aspartate for sustained proliferation.

2OG mimetic tool compounds have been shown to have antiproliferative activity in a small set of cancer cell lines, albeit at high doses (mM) (55), making it difficult to extend these studies to animal models. Nevertheless, our observations suggest that further development of these or similar compounds may have potential therapeutic value if toxicity that may be caused by OGDH inhibition can be tolerated due to the reported association between its reduced activity and neurodegenerative disorders (56). As an alternative to OGDH inhibition, several recent studies have shown that aspartate becomes limiting for cancer cells bearing mutations in succinate dehydrogenase or under conditions of electron transport chain (ETC) suppression, suggesting inhibition of aspartate synthesis as a potential therapeutic strategy in those cancers (33, 34, 38). Furthermore, $NAD^+$ depletion has been explored as a therapeutic option in certain subsets of cancer (57), including IDH1 mutant gliomas, which critically depend on $NAD^+$ availability (58).

Collectively, our observations indicate that oncogenic *PIK3CA* confers a metabolic state that makes cells more sensitive to elevated levels of 2OG, revealing a heightened dependency on aspartate to maintain the malate–aspartate shuttle support for $NAD^+$ regeneration. Further experimental exploration to assess aspartate synthesis, the operation of the malate–aspartate shuttle, or $NAD^+$ regeneration may offer valuable prognostic or therapeutic insights for cancers bearing mutations in *PIK3CA*. Importantly, these observations may extend to other tumors that do not bear mutations in *PIK3CA*, but display a heightened glycolytic use and reliance on efficient $NAD^+$ regeneration. In fact, when we analyzed data from Project Achilles (Fig. 1) we found that other cancer cell lines display sensitivity to OGDH suppression, and it remains to be determined which genetic features drive this dependency. It is plausible that these tumors generally display an increased glycolytic drive and would therefore exhibit comparable vulnerability to increases in 2OG levels. Alternatively, because of the dynamic plasticity of cancer cell metabolism, we could also envision that cell lines that initially exhibited sensitivity to 2OG fluctuation or OGDH suppression could acquire resistance to these insults. One way to achieve resistance would be by a metabolic shift toward increased oxidative metabolism, which would be more glucose efficient, and thus render reduced reliance on the malate–aspartate shuttle for $NAD^+$ regeneration. Hence to prevent therapeutic resistance, cotargeting metabolic pathways involving mitochondrial metabolism may be advantageous, and would represent a confluence of pharmacological opportunities.

## Materials and Methods

**Code Availability.**

***PARIS.*** The GenePattern module PARIS (13) (https://www.broadinstitute.org/achilles/resources) was used for RNMI statistics to generate a list of genes that are preferentially required for proliferation of *PIK3CA* MUT cell lines compared with WT cell lines (Dataset S1). The ATARiS (14) gene level dataset v2.0 was used as a data file (www.broadinstitute.org/achilles/). The mutation annotation file used as classifier was generated using hybrid capture mutation data from the data from the Cancer Cell Line Encyclopedia (https://www.broadinstitute.org/ccle). A total of 85 cell lines (17 *PIK3CA* MUT) were used in the analysis, where cell lines without *PIK3CA* mutation data were removed.

***GSEA.*** GSEA (15) using KEGG 4.0 database was performed on the list of genes identified as required for the survival of *PIK3CA* MUT cell lines using PARIS two-class comparison analysis (13) with the significance cutoff of $P < 0.01$ among *PIK3CA* MUT-associated dependencies. GSEA was performed with 10,000 permutations and a threshold of at least three genes per gene set.

PARIS, ATARiS, and GSEA are publicly available as GenePattern modules (https://genepattern.broadinstitute.org/).

**Cell Proliferation Assays.** Proliferation assays in the presence of shRNAs were performed in 24-well tissue culture dishes where cells were seeded at 10,000–20,000 cells per well. The following day duplicate plates were infected with lentivirus (shRNA); each plate contained four replicate wells for each of the shRNAs used. At 1 d postinfection, one of the duplicate plates was treated with puromycin (selectable marker for shRNAs), and the other plate was refed with fresh media alone. At 4–5 d after infection, plates were fixed with 10% acetic acid/10% ethanol, followed by staining with 0.4% crystal violet/20% ethanol, washed, dried, and then incorporated dye extracted (10% acetic acid) for 96-well format density readings (OD at 595 nm) as a measure of corresponding cell numbers. Fold change in cell numbers was calculated by normalizing to final number of cells in uninfected wells in the absence of puromycin. When doxycycline-inducible shRNAs were used, the proliferation assays were set up similarly, except that doxycycline (0.1 or 1 μg/mL) was added 1 d after seeding, and crystal violet assays performed 96 h after doxycycline addition.

Proliferation assays in the presence of various chemicals or in different growth conditions (e.g., low vs. high nutrients) were performed in the same way, but in the absence of puromycin selection. All drug treatments and nutrient deprivation assays were performed for 96 h. Proliferation assay results are shown as mean values with error bars representing SD from the mean; Student's two-sided *t* test was used to calculate *P* values for experimental two-class comparisons or a one-way ANOVA for multiple comparisons. All proliferation assays were repeated at least three times.

**Immunoblotting.** Protein lysates were resolved on 7.5 or 8–16% polyacrylamide SDS gels (Bio-Rad), transferred onto nitrocellulose membranes (Bio-Rad) using standard wet-transfer procedures, and incubated with primary antibodies as indicated. All immunoblot assays were visualized using a LiCOR Odyssey infrared imager. Quantification of immunoblot signal was performed using LiCOR Odyssey software. For each measurement of signal intensity, the OGDH and α-tubulin signals were adjusted for each lane's background fluorescence, followed by normalization of background-adjusted OGDH signal to background-adjusted α-tubulin signal from the same lane.

**Animal Experiments.** All animal experiments were conducted under animal protocol approved by the Dana-Farber Cancer Institute Institutional Animal Care and Use Committee and in accordance with NIH guidelines. Six-week-old male homozygous NCR-Nu mice (Taconic) were used for xenograft experiments. Briefly, human cancer cell lines expressing dox-inducible shRNA constructs or uninfected human cancer cell lines were injected at three sites each per animal (using 2,000,000 cells per site). Each shRNA cohort contained five mice (maximum 15 tumors per cohort total), based on estimates to reach statistical significance of 80% power in the experiment for at least twofold difference in size and less than 25% SD. Each of 10 animals per experimental group (CONTROL or shOGDH, five animals per individual shRNA) was injected at three injection sites; injection sites that never formed tumors were excluded from the analysis. Dox was administered through food either on the day of injection or upon palpable tumor formation (7–10 d after injection). Tumor size was measured using calipers twice weekly. Tumor size was normalized to initial tumor size on the first day of dox treatment and expressed as percentage of initial size (with initial size set to 100%), or alternatively for initial treatment, represented as direct measured tumor volumes [length × length × width/2 (mm)]. For all animal experiments, statistical significance was calculated using two-sided Student's *t*-test statistics among two experimental groups: shCONTROL (includes uninfected and shRFP) and shOGDH

(includes shOGDH 1714 and 2497); significance of individual experiments is denoted on corresponding graphs using $P$ values, with $P > 0.05$ considered not significant (n.s.). Sample sizes for each experimental group are as follows. Fig. 3*B*, RKO: CONTROL $n = 29$ tumors; shOGDH $n = 27$ tumors. Fig. 3*C*, LS411N: CONTROL $n = 22$ tumors; shOGDH $n = 25$ tumors. Fig. 3*E*, RKO: CONTROL $n = 26$ tumors; shOGDH $n = 26$ tumors. Fig. 3*E*, HCT116: CONTROL $n = 23$ tumors; shOGDH $n = 24$ tumors. Fig. 3*F*, LS411N: CONTROL $n = 21$ tumors; shOGDH $n = 19$ tumors. Fig. 3*F*, HT55: CONTROL $n = 24$ tumors; shOGDH $n = 25$ tumors.

**Materials.** The following antibodies were used: OGDH (HPA020347), DLST (SAB1412704, clone 4D7) and α-tubulin (T9026, clone DM1A) from Sigma Aldrich; p110α (4255) and GAPDH (5174) from Cell Signaling; DLD (sc-365977) and SLC1A3 (C-19) from Santa Cruz; secondary anti-rabbit and anti-mouse IRDye antibodies from LiCOR. Lentiviral shRNAs were obtained from The RNA Consortium (TRC), Broad Institute. Complete sequence information for all shRNA constructs used can be found at the TRC website www.broadinstitute.org/rnai/public/.

Human *SLC1A3* cDNA was in a pMXs vector backbone and had been previously described (33).

The following chemicals were used: L-glutamine, sodium pyruvate (Life Technologies); doxycycline (at final concentration of 0.1 or 1 μg/mL; Clontech); 2-deoxyglucose, dimethyl-2-oxoglutarate, dimethyl succinate, diethyl malate, aminooxyacetic acid, rotenone, oligomycin, antimycin A, phenformin, 2,4-dinitrophenol, carbonyl cyanide 4-(trifluoromethoxy)phenylhydrazone (FCCP), L-aspartic acid (Sigma Aldrich).

The following TRC shRNAs were used: shPIK3CA 2145 TRCN0000039607 (GCTCATTAACTTAACTGACAT); shPIK3CA 3234 TRCN0000010407 (AATGAAAGCTCACTCTGGATT); shOGDH 1714 TRCN0000220904 (CCTGAGTATGAGGAGGAAATT); shOGDH 2497 TRCN0000220905 (GAAGCCAACTTCGACATCAAT); shOGDH 2956 TRCN0000220907 (GACTACGTGAAGCCAAGACTT); shLacZ TRCN0000072231 (CGCTAAATACTGGCAGGCGTT); shLUC TRCN0000072254 (ATGTTTACTACACTCGGATAT); shGFP TRCN0000072186 (TGCCCGACAACCACTACCTGA); and shRFP TRCN0000072212 (CCGTAATGCAGAAGAAGACCA).

The dox-inducible shRNA vector backbone was previously described (59), whereby the inducible shRNAs were generated by cloning annealed hairpin oligos into the AgeI/EcoRI site of pLKO-TO.puro. The OGDH wobble mutant overexpression construct was generated by site-directed mutagenesis of the OGDH wild-type cDNA [obtained from the human ORFeome collection (horfdb.dfci.harvard.edu/hv7/), internal ID 3630] in the pDONR.223 vector (Invitrogen). Five mutations were inserted per targeting shRNA, resulting in 15 total conservative nucleotide substitutions. We used the following primers for site-directed mutagenesis: 1714_TOP: ggtcaaccagcctgaAtaCgaAgaAgaGatttccaagtatgat; 1714_BOTT: atcatacttggaaatCtcTtcTtcGtaTtcaggctggttgacc; 2479_TOP: gccagaccttaaagaGgcAaaTttTgaTatcaatcagctatat; 2479_BOTT: atatagctgattgatAtcAaaAttTgcCtctttaaggtctggc; 2956_TOP: aggctactatgactaTgtAaaAccGagGcttcggaccaccatc; and 2956_BOTT: gatggtggtccgaagCctCggTttTacAtagtcatagtagcct.

Using the Gateway LR reaction (Invitrogen), the wobble OGDH cDNA was moved to pLenti6.3/V5 destination vector (Invitrogen), which was used for subsequent lentivirus production. All cDNA expression constructs are deposited to Addgene.

**Cell Culture.** The following human cancer cell lines were used: HT29, T47D, MDA-MB-453, KM12, HT55, C2BBe1, RKO, GP2D, DLD1, MCF7, SF767, AGS, SKCO1, LS411N, COV362, IGR39, Kuramochi, HCT116, TOV21G, and SU.86.86. These cell lines were obtained from The Cancer Cell Line Encyclopedia (CCLE) - https://www.broadinstitute.org/ccle/home and were originally acquired by CCLE from multiple commercial vendors. Before their use in Project Achilles and subsequent validation experiments, all cell lines were tested for mycoplasma contamination and SNP fingerprinted to confirm their identity (60). All cell lines were cultured in DMEM containing 4.5 g/L glucose (unless indicated otherwise), L-glutamine, and sodium pyruvate (Life Technologies 11995-073), supplemented with penicillin/streptomycin, L-glutamine (4 mM), and 10% FBS. Cell line derivatives expressing dox-inducible shRNAs were cultured in the same media but supplemented with Tet-System Approved FBS from Clontech (tetracycline-free). In experiments in which cells were grown in low glucose (1 g/L) or in reduced or no glutamine, DMEM low glucose (Life Technologies 11885-084) or DMEM no glutamine (Life Technologies 10313-021) were used, respectively.

**Stable Cell Lines.** Cell lines with stable expression of cDNA or shRNAs were generated using lentiviral delivery vectors. Cells were grown on six-well dishes and infected with lentiviruses at high multiplicity of infection. The following day the cell media was replaced with fresh media, trypsinized, transferred to a 10-cm dish and selected with puromycin or blasticidin the day after.

**Metabolite Profiling and Analysis and Glucose Isotope Tracing.** Metabolite extraction was performed as described previously (61). In brief, cells were cultured in log growth phase on 10-cm dishes to ∼70–80% confluence. Two hours before metabolite extraction, cells were refed with fresh media. Cells were then washed with PBS at 37 °C, followed by metabolite extraction by scraping in 80% methanol (on dry ice), insoluble materials collected, two sequential extractions combined and stored at −80 °C. For extracellular lactate quantification, cells were propagated in pyruvate-free media on six-well dishes and at indicated time points following initial refeeding 30 μL of media was harvested per well per sample. Subsequent extracellular metabolite extraction was performed on dry ice by adding methanol to final concentration of 80%, followed by centrifugation to remove insoluble materials (61). Before mass spectrometry, the metabolite extracts were lyophilized, resolubilized in 20 μL of LC/MS grade water, and then analyzed by liquid chromatography tandem mass spectrometry using positive ion/negative ion polarity switching via selected reaction monitoring on a 5500 QTRAP hybrid triple-quadrupole mass spectrometer (AB/SCIEX), as previously described (61). Peaks were integrated using MultiQuant 2.1 data analysis software (AB/SCIEX). Metabolite differences were analyzed by normalizing samples by total levels and comparing replicate samples in groups that satisfy significance of $P < 0.05$ [unpaired two-sided $t$ test with Welch's correction for unequal variance (for two groups) or a one-way ANOVA with multiple comparisons (for more than two groups)].

Glucose isotope tracing was conducted following the same protocol as for unlabeled metabolite profiling. Cells were incubated in regular media for 24 h and then refed with media containing unlabeled 2.25 g/L glucose (half of standard glucose concentration normally used) 24 h before harvesting metabolites. For baseline comparison among cell lines, the media was supplemented with 2.25 g/L [U-$^{13}$C]–glucose 6 h before metabolite isolation. For experiments with dox-inducible OGDH suppression, cells were incubated in the presence of dox for 48 h and refed with media containing dox and unlabeled 2.25 g/L glucose for another 24 h. At 3 h before harvesting metabolites, the media was supplemented with 2.25 g/L [U-$^{13}$C]–glucose.

**Glutamine Isotope Tracing.** Glutamine isotope tracing was conducted on a QExactive benchtop Orbitrap mass spectrometer equipped with an Ion Max source and a HESI II probe, coupled to a Dionex UltiMate 3000 UPLC system (Thermo Fisher Scientific). Cells were incubated in the presence of dox for 72 h and refed with glutamine-free DMEM media supplemented with 1 mM [U-$^{13}C_5$]–glutamine 7 h before harvesting polar metabolites with 80% methanol (with 10 ng/mL valine-$d_8$ as internal standard). Following 10 min vortex at 4 °C and a 10 min spin at 20,800 × $g$, samples were dried under nitrogen gas and resuspended in 100 μL water for analysis. Analysis was performed as previously described (33).

**Bioenergetic Profiling.** Oxygen consumption rate (OCR) and ECAR of intact cells were measured using an XF24 Extracellular Flux Analyzer (Seahorse Bioscience). For OCR measurements, cells were seeded in four replicate wells on Seahorse XF24 cell culture plates in their standard growth media and assayed 24 h later. Two basal OCR measurements were taken in 9-min intervals, followed by sequential injections of 1 μM oligomycin, 4 μM FCCP, and 1 μM antimycin A, taking two measurements at 9-min intervals following each treatment. Following analysis, the cells were trypsinized and counted for each well to normalize the OCR values. For basal ECAR measurements, cells were seeded in four replicate wells on Seahorse XF24 cell culture plates in their standard growth media, but lacking pyruvate. ECAR measurements were performed 24 h later after starving of glucose for 1 h and restimulation with 25 mM glucose for 35 min before the measurement. ECAR values were normalized to cell numbers.

**SYTOX Assay (Cell Death).** Cell death assessment was performed using SYTOX staining (100 nM, SYTOX Green; Molecular Probes) followed by FACS analysis to measure relative SYTOX-positive cells as a function of total cells at 96 h post doxycycline induction of the indicated lentiviral shRNAs.

**Cell Counting (with Trypan Blue Staining).** Following 96 h of propagation in the absence or presence of doxycycline (to induce shRNA expression), cells were trypsinized and analyzed on the ViCell Analyzer for total cell numbers and percent of viable cells (Beckman). Trypan blue exclusion was used as an indicator of cell viability.

**Cell-Cycle Analysis.** Following 72 h of propagation in the presence of doxycycline (to induce shRNA expression), BrdU was added for 2 h, after which the cells where trypsinized and stained with anti–BrdU-FITC antibody and 7AAD, following the manufacturer's protocol (BD Pharmingen catalog no. 559619). The cells were then analyzed on a BD FACS Canto instrument and analyzed using FlowJo software.

**ACKNOWLEDGMENTS.** We thank Min Yuan and Susanne Breitkopf for help with mass spectrometry experiments; Jack Lee, Jenna Geddes, and Nick Giovannone for FACS support; and Drs. Pere Puigserver, Chao (Daisy) Dai, Ji Li, and members of W.C.H.'s laboratory for scientific discussions. This work was partially supported by NIH Grants U01 CA176058 (to W.C.H.), R01 CA130988 (to W.C.H.), U54 CA112962 (to W.C.H.), P01 CA142536 (to W.C.H.), K22 CA193660 (to K.B.), P01 CA120964 (to J.M.A.), and P30 CA006516 (to J.M.A.); Susan G. Komen Foundation Grant PDF12230602 (to N.I.); the Terri Brodeur Breast Cancer Foundation (N.I.), a Sidney Kimmel Scholar Grant (to K.B.); Damon Runyon Cancer Research Foundation HHMI Fellowship (to N.K.); Department of Defense Grant W81XWH-15-1-0337 (to E.F.); and the H. L. Snyder Foundation (W.C.H.).

1. Samuels Y, et al. (2004) High frequency of mutations of the PIK3CA gene in human cancers. *Science* 304:554.
2. Vanhaesebroeck B, Vogt PK, Rommel C (2010) PI3K: From the bench to the clinic and back. *Curr Top Microbiol Immunol* 347:1–19.
3. Samuels Y, et al. (2005) Mutant PIK3CA promotes cell growth and invasion of human cancer cells. *Cancer Cell* 7:561–573.
4. Bendell JC, et al. (2012) Phase I, dose-escalation study of BKM120, an oral pan-Class I PI3K inhibitor, in patients with advanced solid tumors. *J Clin Oncol* 30:282–290.
5. Janku F, et al. (2013) PIK3CA mutation H1047R is associated with response to PI3K/AKT/mTOR signaling pathway inhibitors in early-phase clinical trials. *Cancer Res* 73:276–284.
6. Ganesan P, et al. (2013) Target-based therapeutic matching in early-phase clinical trials in patients with advanced colorectal cancer and PIK3CA mutations. *Mol Cancer Ther* 12:2857–2863.
7. Taha C, et al. (1999) Opposite translational control of GLUT1 and GLUT4 glucose transporter mRNAs in response to insulin. Role of mammalian target of rapamycin, protein kinase b, and phosphatidylinositol 3-kinase in GLUT1 mRNA translation. *J Biol Chem* 274:33085–33091.
8. Brachmann SM, Ueki K, Engelman JA, Kahn RC, Cantley LC (2005) Phosphoinositide 3-kinase catalytic subunit deletion and regulatory subunit deletion have opposite effects on insulin sensitivity in mice. *Mol Cell Biol* 25:1596–1607.
9. Deberardinis RJ, Lum JJ, Thompson CB (2006) Phosphatidylinositol 3-kinase-dependent modulation of carnitine palmitoyltransferase 1A expression regulates lipid metabolism during hematopoietic cell growth. *J Biol Chem* 281:37372–37380.
10. Hu H, et al. (2016) Phosphoinositide 3-kinase regulates glycolysis through mobilization of aldolase from the actin cytoskeleton. *Cell* 164:433–446.
11. Pusapati RV, et al. (2016) mTORC1-dependent metabolic reprogramming underlies escape from glycolysis addiction in cancer cells. *Cancer Cell* 29:548–562.
12. Cheung HW, et al. (2011) Systematic investigation of genetic vulnerabilities across cancer cell lines reveals lineage-specific dependencies in ovarian cancer. *Proc Natl Acad Sci USA* 108:12372–12377.
13. Cowley GS, et al. (2014) Parallel genome-scale loss of function screens in 216 cancer cell lines for the identification of context-specific genetic dependencies. *Sci Data* 1:140035.
14. Shao DD, et al. (2013) ATARiS: Computational quantification of gene suppression phenotypes from multisample RNAi screens. *Genome Res* 23:665–678.
15. Subramanian A, et al. (2005) Gene set enrichment analysis: A knowledge-based approach for interpreting genome-wide expression profiles. *Proc Natl Acad Sci USA* 102:15545–15550.
16. Bunik VI, Fernie AR (2009) Metabolic control exerted by the 2-oxoglutarate dehydrogenase reaction: A cross-kingdom comparison of the crossroad between energy production and nitrogen assimilation. *Biochem J* 422:405–421.
17. Brachmann SM, et al. (2012) Characterization of the mechanism of action of the pan class I PI3K inhibitor NVP-BKM120 across a broad range of concentrations. *Mol Cancer Ther* 11:1747–1757.
18. Csibi A, et al. (2013) The mTORC1 pathway stimulates glutamine metabolism and cell proliferation by repressing SIRT4. *Cell* 153:840–854.
19. Csibi A, et al. (2014) The mTORC1/S6K1 pathway regulates glutamine metabolism through the eIF4B-dependent control of c-Myc translation. *Curr Biol* 24:2274–2280.
20. Buzzai M, et al. (2005) The glucose dependence of Akt-transformed cells can be reversed by pharmacologic activation of fatty acid beta-oxidation. *Oncogene* 24:4165–4173.
21. Furet P, et al. (2013) Discovery of NVP-BYL719 a potent and selective phosphatidylinositol-3 kinase alpha inhibitor selected for clinical evaluation. *Bioorg Med Chem Lett* 23:3741–3748.
22. Doherty JR, Cleveland JL (2013) Targeting lactate metabolism for cancer therapeutics. *J Clin Invest* 123:3685–3692.
23. Wuntch T, Chen RF, Vesell ES (1970) Lactate dehydrogenase isozymes: Further kinetic studies at high enzyme concentration. *Science* 169:480–481.
24. Gutfreund H, Cantwell R, McMurray CH, Criddle RS, Hathaway G (1968) The kinetics of the reversible inhibition of heart lactate dehydrogenase through the formation of the enzyme-oxidized nicotinamide-adenine dinucleotide-pyruvate compounds. *Biochem J* 106:683–687.
25. Lumeng L, Bremer J, Davis EJ (1976) Suppression of the mitochondrial oxidation of (–)-palmitylcarnitine by the malate-aspartate and alpha-glycerophosphate shuttles. *J Biol Chem* 251:277–284.
26. Williamson JR, Jakob A, Refino C (1971) Control of the removal of reducing equivalents from the cytosol in perfused rat liver. *J Biol Chem* 246:7632–7641.
27. Barron JT, Gu L, Parrillo JE (1998) Malate-aspartate shuttle, cytoplasmic NADH redox potential, and energetics in vascular smooth muscle. *J Mol Cell Cardiol* 30:1571–1579.
28. Tennant DA, et al. (2009) Reactivating HIF prolyl hydroxylases under hypoxia results in metabolic catastrophe and cell death. *Oncogene* 28:4009–4021.
29. Carey BW, Finley LW, Cross JR, Allis CD, Thompson CB (2015) Intracellular α-ketoglutarate maintains the pluripotency of embryonic stem cells. *Nature* 518:413–416.
30. Eto K, et al. (1999) Role of NADH shuttle system in glucose-induced activation of mitochondrial metabolism and insulin secretion. *Science* 283:981–985.
31. Mullen AR, et al. (2014) Oxidation of alpha-ketoglutarate is required for reductive carboxylation in cancer cells with mitochondrial defects. *Cell Reports* 7:1679–1690.
32. Yang H, et al. (2015) SIRT3-dependent GOT2 acetylation status affects the malate-aspartate NADH shuttle activity and pancreatic tumor growth. *EMBO J* 34:1110–1125.
33. Birsoy K, et al. (2015) An essential role of the mitochondrial electron transport chain in cell proliferation is to enable aspartate synthesis. *Cell* 162:540–551.
34. Sullivan LB, et al. (2015) Supporting aspartate biosynthesis is an essential function of respiration in proliferating cells. *Cell* 162:552–563.
35. Cairns RA, Mak TW (2013) Oncogenic isocitrate dehydrogenase mutations: Mechanisms, models, and clinical opportunities. *Cancer Discov* 3:730–741.
36. Tomlinson IP, et al.; Multiple Leiomyoma Consortium (2002) Germline mutations in FH predispose to dominantly inherited uterine fibroids, skin leiomyomata and papillary renal cell cancer. *Nat Genet* 30:406–410.
37. Baysal BE, et al. (2000) Mutations in SDHD, a mitochondrial complex II gene, in hereditary paraganglioma. *Science* 287:848–851.
38. Cardaci S, et al. (2015) Pyruvate carboxylation enables growth of SDH-deficient cells by supporting aspartate biosynthesis. *Nat Cell Biol* 17:1317–1326.
39. Chatterjee A, Mambo E, Sidransky D (2006) Mitochondrial DNA mutations in human cancer. *Oncogene* 25:4663–4674.
40. Son J, et al. (2013) Glutamine supports pancreatic cancer growth through a KRAS-regulated metabolic pathway. *Nature* 496:101–105.
41. Yun J, et al. (2015) Vitamin C selectively kills KRAS and BRAF mutant colorectal cancer cells by targeting GAPDH. *Science* 350:1391–1396.
42. Wise DR, et al. (2008) Myc regulates a transcriptional program that stimulates mitochondrial glutaminolysis and leads to glutamine addiction. *Proc Natl Acad Sci USA* 105:18782–18787.
43. Lien EC, et al. (2016) Glutathione biosynthesis is a metabolic vulnerability in PI(3)K/Akt-driven breast cancer. *Nat Cell Biol* 18:572–578.
44. Elstrom RL, et al. (2004) Akt stimulates aerobic glycolysis in cancer cells. *Cancer Res* 64:3892–3899.
45. Allen EL, et al. (2016) Differential aspartate usage identifies a subset of cancer cells particularly dependent on OGDH. *Cell Reports* 17:876–890.
46. Hao Y, et al. (2016) Oncogenic PIK3CA mutations reprogram glutamine metabolism in colorectal cancer. *Nat Commun* 7:11971.
47. Geissler A, Kanamori K, Ross BD (1992) Real-time study of the urea cycle using 15N n.m.r. in the isolated perfused rat liver. *Biochem J* 287:813–820.
48. Nelson SW, Binkowski DJ, Honzatko RB, Fromm HJ (2005) Mechanism of action of *Escherichia coli* phosphoribosylaminoimidazolesuccinocarboxamide synthetase. *Biochemistry* 44:766–774.
49. Davidson JN, Chen KC, Jamison RS, Musmanno LA, Kern CB (1993) The evolutionary history of the first three enzymes in pyrimidine biosynthesis. *BioEssays* 15:157–164.
50. Consigli RA, Ginsberg HS (1964) Control of aspartate transcarbamylase activity in type 5 adenovirus-infected HeLa cells. *J Bacteriol* 87:1027–1033.
51. Tapiero H, Mathe G, Couvreur P, Tew KD (2002) I. Arginine. *Biomed Pharmacotherapy* 56:439–445.
52. Huang YZ, Knox EW (1975) Glutamine-dependent asparagine synthetase in fetal, adult and neoplastic rat tissues. *Enzyme* 19:314–328.
53. Kirsch JF, et al. (1984) Mechanism of action of aspartate aminotransferase proposed on the basis of its spatial structure. *J Mol Biol* 174:497–525.
54. Jacobo-Molina A, Peterson R, Yang DC (1989) cDNA sequence, predicted primary structure, and evolving amphiphilic helix of human aspartyl-tRNA synthetase. *J Biol Chem* 264:16608–16612.
55. Bunik V, et al. (2016) Inhibition of mitochondrial 2-oxoglutarate dehydrogenase impairs viability of cancer cells in a cell-specific metabolism-dependent manner. *Oncotarget* 7:26400–21.
56. Trofimova LK, et al. (2012) Consequences of the α-ketoglutarate dehydrogenase inhibition for neuronal metabolism and survival: Implications for neurodegenerative diseases. *Curr Med Chem* 19:5895–5906.
57. Galli U, et al. (2013) Medicinal chemistry of nicotinamide phosphoribosyltransferase (NAMPT) inhibitors. *J Med Chem* 56:6279–6296.
58. Tateishi K, et al. (2015) Extreme vulnerability of IDH1 mutant cancers to NAD+ depletion. *Cancer Cell* 28:773–784.
59. Wiederschain D, et al. (2009) Single-vector inducible lentiviral RNAi system for oncology target validation. *Cell Cycle* 8:498–504.
60. Barretina J, et al. (2012) The Cancer Cell Line Encyclopedia enables predictive modelling of anticancer drug sensitivity. *Nature* 483:603–607.
61. Yuan M, Breitkopf SB, Yang X, Asara JM (2012) A positive/negative ion-switching, targeted mass spectrometry-based metabolomics platform for bodily fluids, cells, and fresh and fixed tissue. *Nat Protoc* 7:872–881.